Materials Science Forum
ISSN: 1662-9752, Vol. 1187, pp 99-112
doi:10.4028/p-a49Y50

Submitted: 2025-12-22
Revised: 2026-02-23
Accepted: 2026-02-23
Online: 2026-04-17

Design and Manufacturing of Complex Geometry PEEK Component through Fused Filament Fabrication

Niccolo Burattini[1,a*], Luana Bottini[1,b], Domenico Corapi[1,c], Alberto Boschetto[1,d]

[1]Sapienza University of Rome, via Eudossiana 18, 00184, Rome, Italy

[a*]niccolo.burattini@uniroma1.it, [b]luana.bottini@uniroma1.it, [c]domenico.corapi@uniroma1.it, [c]alberto.boschetto@uniroma1.it

Keywords: fused filament fabrication, PEEK, digital image analysis

Abstract. Complex geometry components fabricated through Fused Filament Fabrication in polyether ether ketone exhibit very interesting performances, but they are very difficult to predict. Non-standard mechanical tests allow for estimating a global structural response and do not provide local information about the failure evolution. This work investigates the integration of a Digital Image Processing method with non-standard mechanical test to improve the knowledge of the component performance through the tracking and the analysis of local failures. This way, a targeted redesign of the component can be provided: in this work the component was modified at manufacturing stage by changing the Fused Filament Fabrication infill, and at optimization stage by employing a stress line approach for locally densifying the interior.

Introduction

The growing industrial demand for flexibility and geometric complexity has driven the proliferation of Additive Manufacturing (AM) technologies. Among these technologies, Fused Filament Fabrication (FFF) has emerged due to its relative simplicity, low cost, and material versatility. FFF offers a broader range of printable materials, from easy-to-print polymers to high-performance engineering thermoplastics with superior mechanical properties, including polyetherimide, and Polyaryl Ether Ketone (PAEK).

PAEK is a family of high-performance thermoplastic polymers, consisting of an aromatic backbone molecular chain, interconnected by ketone and ether functional groups. One famous member of this group is Polyether Ether Ketone (PEEK). It can be employed to fabricate functional components aiming to substitute metallic alloy. Typically, PEEK components are processed via traditional injection molding and extrusion, nonetheless recent advancements enabled the manufacturing through FFF [1]. This high-value polymer is widely used in biomedical field for its biocompatibility [2], finding application in areas such as craniomaxillofacial reconstruction [3], joint replacement [4], and arthroscopy [5]. PEEK is considered a low-flammable material due to its high thermal stability, resistance to autoignition, and self-extinguishing behavior [6]. In addition, it does not exhibit outgassing phenomena and it is resistant to relatively high temperature, making it suitable for the aerospace industry [7]. In the automotive sector, the weight reduction allowed by high performance polymers and composite materials is crucial for decreasing fuel consumption. Furthermore, fabrication through AM provides extreme flexibility while reducing tooling and prototyping costs [8]. Although AM offers these advantages, fabrication times can be relatively long; for this reason, tools for predicting static and fatigue behavior are being investigated [9], together with the influence of process parameters [10]. Due to its intrinsic anisotropy and lack of homogeneity, the simulation of AMed parts remains challenging. Finite Element Analysis (FEA) materials databases include isotropic materials, which struggle to obtain reliable results when applied to layer-by-layer manufactured, anisotropic components. FEA simulation is a simplified model which assumes full solid body, whereas FFFed parts are composed of bonded filaments. As reported in [11], an isotropic model can predict with a certain reliability the mechanical behaviors in the elastic region; however, when the plastic deformation occurs, orthotropic material properties become more appropriate.

Although simulations struggle to achieve reliable results, their accuracy can be enhanced through calibrated models [12]. Both for calibrating numerical models and to compensate for the reliability

of FEA, experimental mechanical testing is unavoidable. Standard mechanical tests are not always representative of the behavior of complex geometries which are one of the main reasons for choosing AM technologies. Mechanical tests on custom-geometry specimens provide high quality information on AMed components. Optimizing the mechanical properties of parts fabricated using FFF usually requires a considerable number of test samples; long testing campaigns undermine the advantages of AM such as flexibility. Moreover, PEEK and other high-performance thermoplastics are relatively expensive. For these reasons, it is essential to extract maximum amount of information from each individual non-standard test.

Digital Image Processing (DIP) techniques have been exploited by researchers in the past half of century for many application fields [13]. The universal access of cameras has grown, making video data exponentially increase. The Video Object Tracking and Image Keypoint Detection are now widely used for precise localization in the fields of autonomous driving, augmented reality. Smart Factory, Industry 5.0 and Smart Cities pumped up new algorithms developments striving to efficiently determine features in manufacturing processes and structures [14]. The remote monitoring of structure features enables displacement measurement at multiple locations at a time, contrary to the contact-based sensors that allow detecting the displacement only at the places of their physical location [15]. Advancements in processing capability have led to the growing popularity of convolutional neural networks allowing for classification and detection measurements of geometrical features and damages. However, they require the availability of large datasets and a number of experimental tests accordingly. Therefore, they are not suitable whereas the aim is to return information on a single test characterized by unique conditions and behavior. DIP feature detection, is based on image keypoints and numerous registration algorithms for determining keypoints were developed but it is still difficult to build a universal framework. These algorithms are called detectors and include: Feature from Accelerated Segment Test, Binary Robust Invariant Scalable Keypoints, Speed Up Robust Feature (SURF), and many other [16]. Video Object Tracking, also known as Visual Object Tracking, faces many challenges, such as target occlusion, target deformation and so on. [17]. Observation-Centric Simple Online and Real-time Tracking employs a Kalman Filter to tracks found by Hungarian algorithm. This allows a prediction of the next state, called state of propagation, and the possible association is evaluated by Kalman estimators.

In this work the application of DIP to the rapid testing is presented. The aim is to measure displacements in a FFF part under deformation to provide feedback about the effects of the combination between geometry design and manufacturing.

The lightening of mechanical parts can be achieved through Topological Optimization (TO). This methodology utilizes a density-based formulation, such as the Solid Isotropic Material with Penalization (SIMP). Through the iterative execution of sensitivity analyses on a target objective, typically the reduction of global compliance to enhance structural rigidity under a fixed volume budget, the algorithm eliminates superfluous material and concentrates it along critical stress trajectories [18]. Another approach could consist in designing for stiffness by considering the force flow lines that originate in the principal stress directions [19]. AM technologies give full play to the complex geometries integrated with the force-flow based design to maximize structural efficiency [20]. This method, known as Michell Trusses Design method, found application in mechanical elements design indicating a significant reduction in lightweight structural modelling [21]. In [22] the weight and the vibration response of a gear are optimized by offsetting the principal stress lines. The method known as "Stress Line Additive Manufacturing" (SLAM) reconsiders the FFF technique by adding material along the principal stresses [23].

This paper explores the combination of non-standard mechanical test and DIP and its capability to improve the information through identification of local failure mechanisms. Non-standard mechanical test provides only the global structural response, whilst the integration with DIP enables the detection of local critical conditions, allowing direct modifications on specific features at the redesign phase. This work investigates how improved mechanical performance can be achieved through different manufacturing strategies, comparing a rectilinear infill, acting homogenously across the bulk material, or with a SLAM design approach which enables local modifications in regions identified as critical by the integrated analysis method.

Materials & Methods

Design. The investigated component is an electronic device support mounted on the motorbike of the Sapienza motor student. Its original shape and topological optimized one are shown in Fig. 1a and 1b respectively. The TO design was provided by using Inspire v.2025 Personal Edition and considering the system of loads and constraints characterizing the specific application.

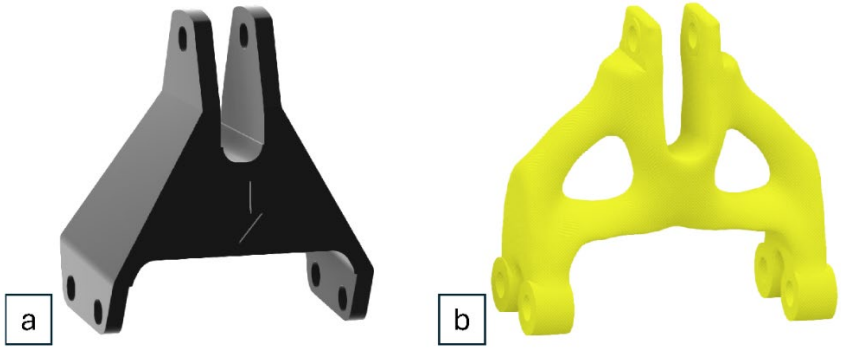

Fig. 1 Original component (a), component optimized by TO (b)

This traditional approach exhibits lack of effectiveness since the known anisotropy of FFFed parts is not considered in the TO material definition and simulation as well. In fact, the FFF part is composed of a skin made by contours and the inner part made by infill strategies. The SLAM approach was undertaken by developing an original code in McNeel's Grasshopper, a visual programming environment for the 3D modeler Rhinoceros [24]. The aim was to apply parametric geometric modelling and mechanical simulation techniques to determine a locally variant filling hatching using the principal stress flow lines criterion. The logic underlying this architecture is represented by the workflow summarized in Fig. 2.

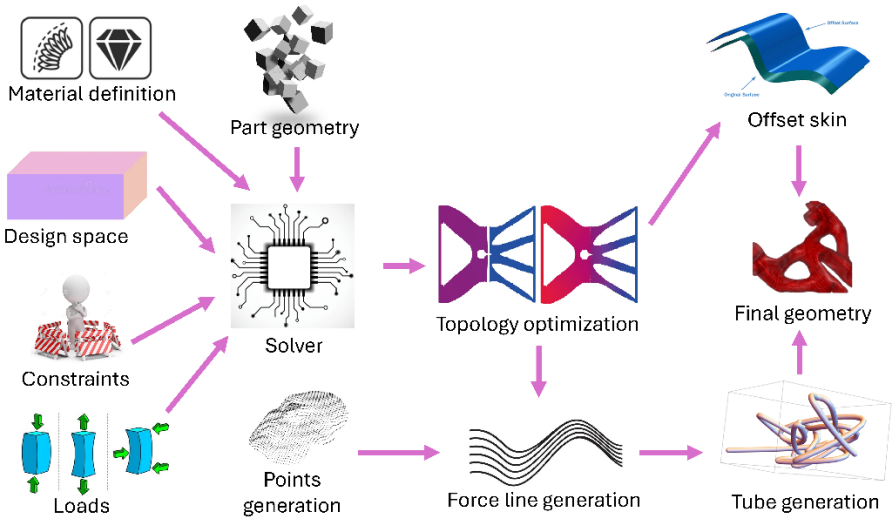

Fig. 2 Workflow of the architecture for the development of a geometry based on SLAM approach.

A number of attributes are given in input to the solver: material definition, such as modulus of elasticity, Poisson ratio, density, yield strength; the design space, i.e., the portion of the three-dimensional domain that defines the shape of the mechanical component that will actually be processed by the topological optimization algorithm; the domain on which the loads are applied; the definition of the constrained domain in terms of suppressed displacements and rotations. A specified number of points are generated in random positions and used to trace the force lines; the traces are transformed into manufacturable tubes of the desired diameter. An external skin, with a parameterized thickness, that acts as a closed container of the force lines is created. Finally, both the internal tube

structures and the outer skin are assembled in a single complex geometry. The Fig. 3 shows the whole Grasshopper structure of the described workflow.

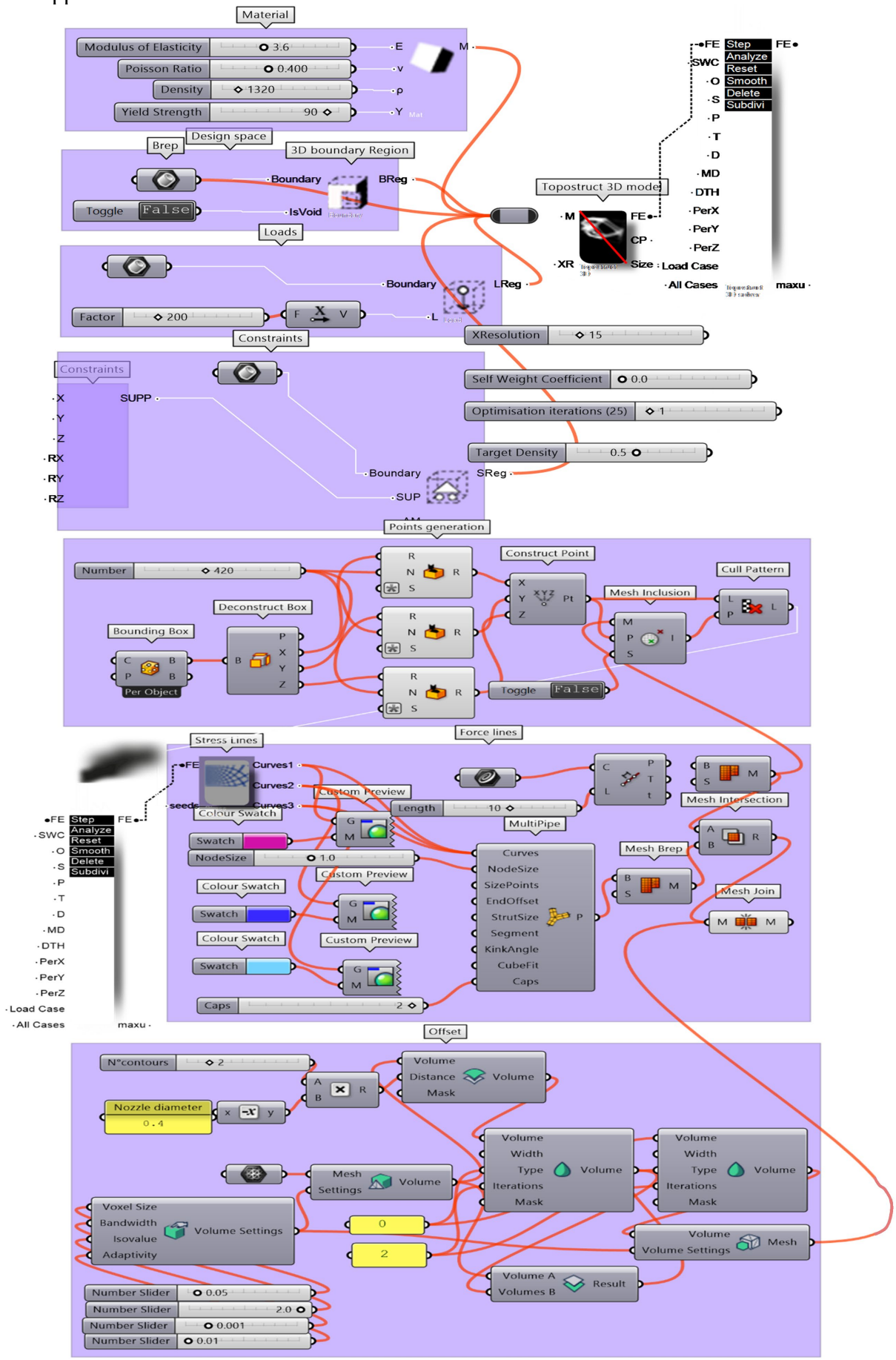

Fig. 3 Grasshopper architecture for developing the part geometry according with SLAM approach

Fabrication. The specimens were fabricated using a CreatBot PEEK-300 printer (Henan Creatbot Technology Limited, No. 150 Lamei Road, Zhongyuan District, Zhengzhou City, Henan Province, China), employing 1.75 mm CreatBot PEEK filament as feedstock material. According to the manufacturer, the mechanical properties of the filament are tensile: strength 100 MPa, tensile modulus 3720 MPa, flexural strength 128 MPa, and flexural modulus 2700 MPa. The glass transition temperature of the stock material, measured by Differential Scanning Calorimetry, is 143 °C and increases up to 158 °C after fabrication. The nozzle, chamber, and platform temperatures were set to 440 °C, 100 °C, and 150 °C respectively. Under these conditions, the resulting crystallinity is within the range of 27.9-29.9% for edge regions and 29.6-31.1% for the internal regions of the component. Other relevant process parameters include the layer thickness (0.15 mm), nozzle diameter (0.4 mm), and extrusion speed (20 mm/s). For slicing operations and process parameter selection, the CreatBot Creatware was used. Three infill strategies were investigated. The first consists of a rectilinear infill with variable bulk densities, namely 5%, 10%, and 25%. A second component type was developed according to the SLAM design. The number of contour lines is two and kept unchanged. In Table 1 the list of specimen codes is reported together with the fabrication strategies:

Table 1 Specimen codes, infill densities, and infill strategies

Specimen code	Infill density [%]	Infill strategy
27 – PEEK – F05	5	Rectilinear
20 – PEEK – F10	10	Rectilinear
22 – PEEK – F10	10	Rectilinear
25 – PEEK – F25	25	Rectilinear
26 – PEEK – F25	25	Rectilinear
23 – PEEK – ASY	-	SLAM
28 – PEEK – ASY	-	SLAM
24 – PEEK – SYM	-	SLAM
29 – PEEK – SYM	-	SLAM

Non-standard mechanical test and DIP. A non-standard mechanical test was developed to measure the mechanical resistance of the manufactured components. A S Beam Load Cell model LCM103B-250 (OMEGA Engineering 1 Omega Drive, Northbank, Irlam, Manchester, M44 5BD, United Kingdom) and a Soway SDVB20 LVDT sensor (Soway Tech Limited, No.28 Xinfeng Road Potoubei Ailian Longgang Shenzhen China 518000) were adopted for measuring the exerted force and the displacement respectively. A stepper motor and a gear box were used to provide the lateral force for deforming the component. A 950 lm white led spotlight was positioned beside a semi-transparent acrylic wall. Layout elements are shown in Fig. 4. A GoPro Hero12 was used to acquire the component during the test. The resolution was set at 3840x2160 pixel^2 and the video was captured at 50 frame/s and coded in High Efficient Video Coding (HEVC) according to ISO/IEC 23008-2 MPEG-H Part 2 [25]. The signals of the load cell and the displacement sensor were acquired by a National Instruments NI6221 (National Instruments Corporation 11500 North Mopac Expressway, Austin, TX 78759 USA), programmed in Labview 18.3.

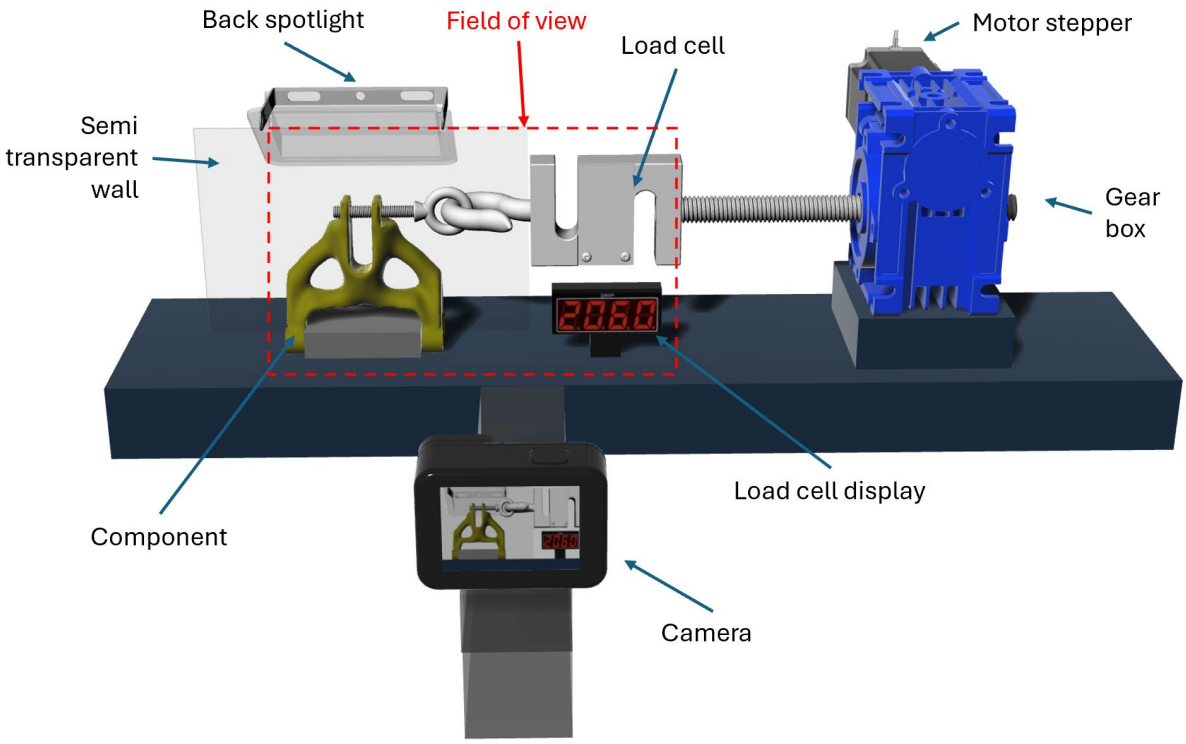

Fig. 4 Layout of the non-standard test device

Force and displacement and video data were processed in Mathematica Wolfram 14.3. Video and array data were synchronized by capturing in the shown field of view the component and the load cell display.
The HEVC videos were completely managed in Mathematica environment by embedding v6.1.1 "Von Neumann" FFMPEG video codec support. The videos were processed accordingly to the workflow shown in Fig. 5.

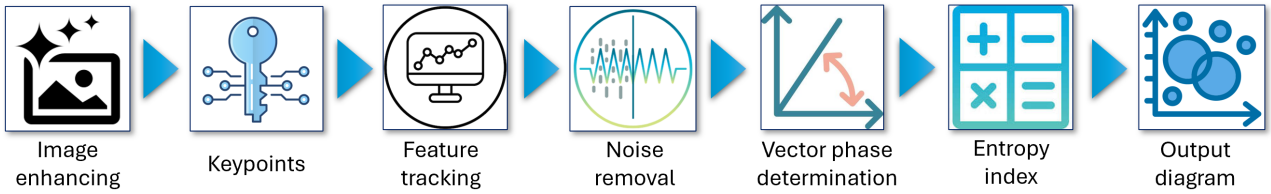

Fig. 5 DIP workflow

The original images were improved by means of edge enhancement. An increased noise is observed in nearly uniform regions leading to a reduced local contrast at boundaries. Therefore, a sharpening [13] was applied through a Laplacian operator which highlights local contrasted areas and suppresses smooth gradients. The image keypoints were found by using SURF algorithm and setting the strength constrain to the minimum confidence of 0.005 which typically led to about 30 elements. These points were employed in the visual tracking algorithms to find their trajectories during the deformation. For the purpose an Observation-Centric Simple Online and Realtime Tracking was adopted. It is based on classic Kalman assumptions of linear motion and Gaussian noise that can be adequate for the slow dynamic of these measurements.
A filtering was adopted to avoid noises coming from image errors and algorithm issues. The original image was convolved as in Eq. 1:

$$F(x,y) = \sum_i \sum_j f(x+u, y+v), G(u,v) \tag{1}$$

where $f(x,y)$ is the original image pixel at coordinates x and y, $F(x,y)$ is the filtered image pixel at the same coordinates, u and v are local spatial variables, and $G(x,y)$ is the Gaussian blur with standard deviation σ as reported in Eq. 2:

$$G(x,y) = \frac{1}{2\pi\sigma} e^{-\frac{x^2+y^2}{2\sigma^2}} \tag{2}$$

Each trajectory was processed to find the displacement vector fields. The vector phase $\theta_i^{(k)}$ calculated on the *i-th* point coordinates $x_i^{(k)}, y_i^{(k)}$ of the *k-th* trajectory was calculated as in Eq. 3:

$$\theta_i^{(k)} = Atan2\left(y_i^{(k)} - y_{i-1}^{(k)}, x_i^{(k)} - x_{i-1}^{(k)}\right) \tag{3}$$

where *Atan2(x,y)* is the inverse trigonometric function that returns the arctangent of two arguments allowing to determine unambiguously the correct quadrant among all four ones. Trajectories were smoothed by applying a Gaussian filter characterized by 12.5 px standard deviation to avoid errors coming from local reflection and noises.
In this work an indicator is proposed to highlight undesired conditions of the slope trend of each trajectory associated with critical deformation. Under the hypothesis that smooth deformations are characterized by a linear relationship of slope trend, the regression equation of the *k-th* trajectory is reported in Eq. 4:

$$\hat{y}^{(k)}(x) = \frac{\sum_j (x_i^{(k)} - \bar{x}_i^{(k)})(y_i^{(k)} - \bar{y}_i^{(k)})}{\sum_j (x_i^{(k)} - \bar{x}_i^{(k)})^2} x + \bar{y}^{(k)} - \frac{\sum_j (x_i^{(k)} - \bar{x}_i^{(k)})(y_i^{(k)} - \bar{y}_i^{(k)})}{\sum_j (x_i^{(k)} - \bar{x}_i^{(k)})^2} \bar{x}^{(k)} \tag{4}$$

where $\hat{y}^{(k)}(x)$ is the fitted value at $\bar{x}^{(k)}$ and $\bar{y}^{(k)}$ are the mean value of coordinate $x_i^{(k)}$ and $y_i^{(k)}$ respectively.
The estimated error standard deviation is considered as an unbiased indicator of the slope variability from its linear regression. In Eq. 5, the veer index is defined as the root square of the mean square error (MSE):

$$\xi^{(k)} = \sqrt{MSE^{(k)}} = \sqrt{\frac{\sum (y_i^{(k)} - \hat{y}_i^{(k)})^2}{n^{(k)}}} \tag{5}$$

where $n^{(k)}$ is the number of points of the *k-th* trajectory.
This index is expected to be low as a regular deformation trend occurs on the specified *k-th* trajectory. Conversely, a break-down behavior is characterized by a big value.

Results

The load-displacement curve of the 22-PEEK-F10 shown in Fig. 6a is a representative structural response of the specimen with respect to the imposed displacement. The first interval can be described as a quasi-elastic stage. However, this region does not represent a purely elastic structural response, as local damages already occurred. This damage includes local plastic deformation and failure mechanisms such as delamination, filament debonding, and the initiation of internal microcracks. These phenomena are further supported by the frequent audible fracture events. The second stage begins after 4.83 mm, when significant local structural failures occur. In this stage, the overall response is characterized by a load plateau, where the structure reaches new equilibrium states followed by successive failure events. In particular, the first peak load is reached at 882.7 N for an imposed displacement of 4.8 mm; the maximum peak is reached in the second stage at 904.4 N corresponding to 9.0 mm displacement; the length of the load plateau is equal to 3.5 mm. The ratio between the final load of the first stage and the corresponding displacement is the stiffness of the

structure, in this case 182.6 N/mm. By analyzing the achieved video, some events denote some critical zones and are subjected to local failures. The points indicated in Fig. 6a are related to those events. In Fig. 6b and in Fig. 6c the selected zones are captured just one second before the event and at the failure respectively. Several damage types can be observed: cracks occur on the surface; a feature markedly rotates with respect to the surrounding elements; a local bump formation; final break on the top coupling holes.

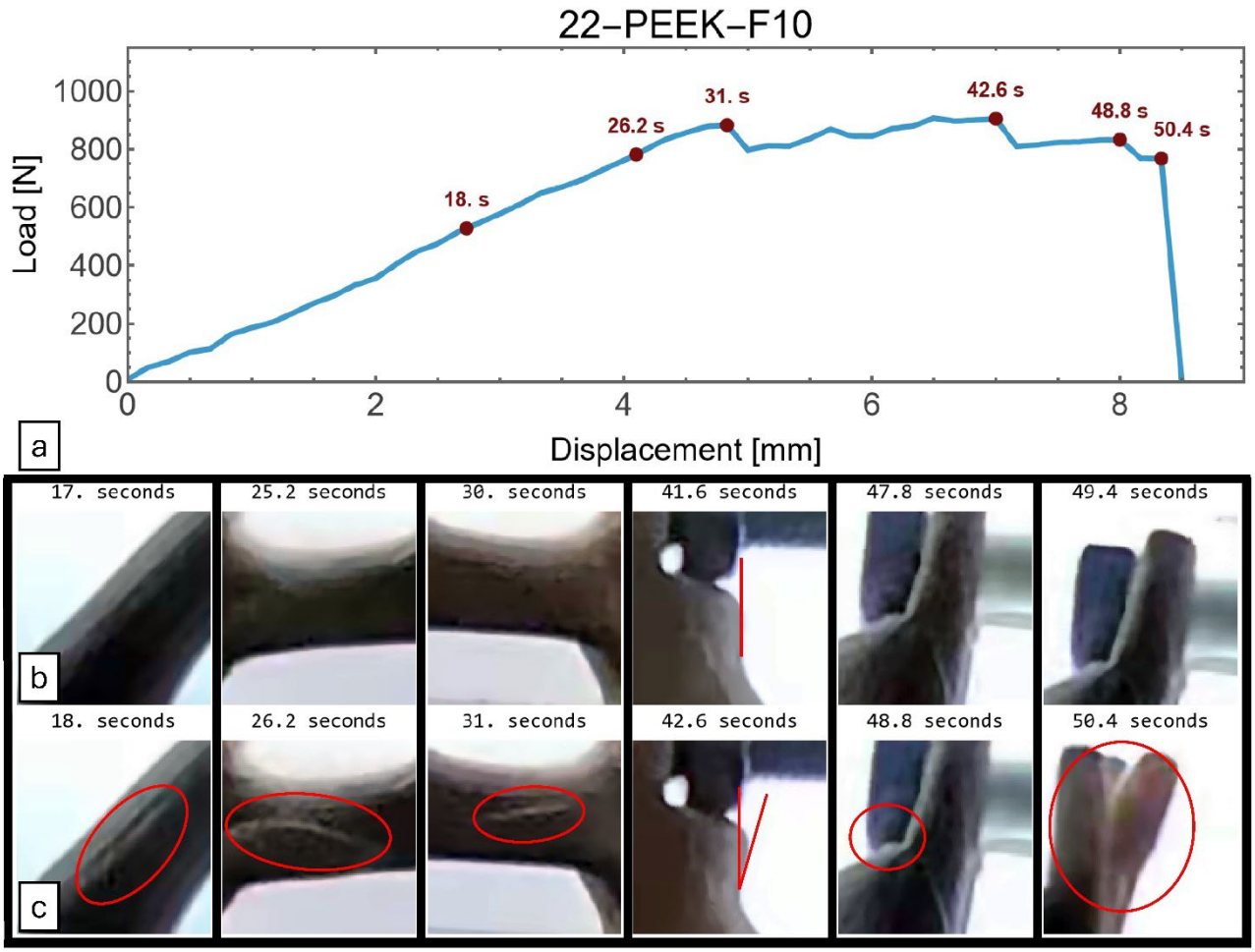

Fig. 6 Load-displacement curve of 22-PEEK-F10 (a), array of local failures one second before the event (b), array of local failures after the event (c)

These quantitative observations highlight the need for automatic DIP technique to quantitatively analyzed each local deformation/failure overall the video frames of the test. The Fig. 7 shows the results of the application of the DIP steps developed in this work. The original image (Fig. 7a) was enhanced by using Laplacian operator. The contrast at edges is well evident in Fig. 7b and in the false colors applied to the upper right quadrants of both images. The image key points are shown in Fig. 7c. The selected SURF algorithm is based on descriptors numerically robust against translation, rotation, and scale changes. The outcomes highlight how specific image features such as shape, contrast and orientation are considered: the indicated points are represented by their confidence (i.e., the radius of the circle), their orientation (the segment inside the circle), and the sign (if the key point is lighter than its surroundings is colored in red else in yellow). Such data allowed to determine robust points to be used for the object tracking and obtain the tracks reported in Fig. 7d. Each track was smoothed by means of a Gaussian filter and the veer indexes were calculated. Fig. 7e points out how the upper curves are near linear hence the variation of the vector angles is low accordingly. As opposed, the behaviors of the tracks in the bottom are nonlinear, highlighting a critical trend in the deformation thus exhibiting a higher veer index. The final representation of the calculated indexes is

shown in Fig. 7f. It can be noticed that two of the previously manually detected zones described in Fig. 6c are markedly evidenced by this methodology.

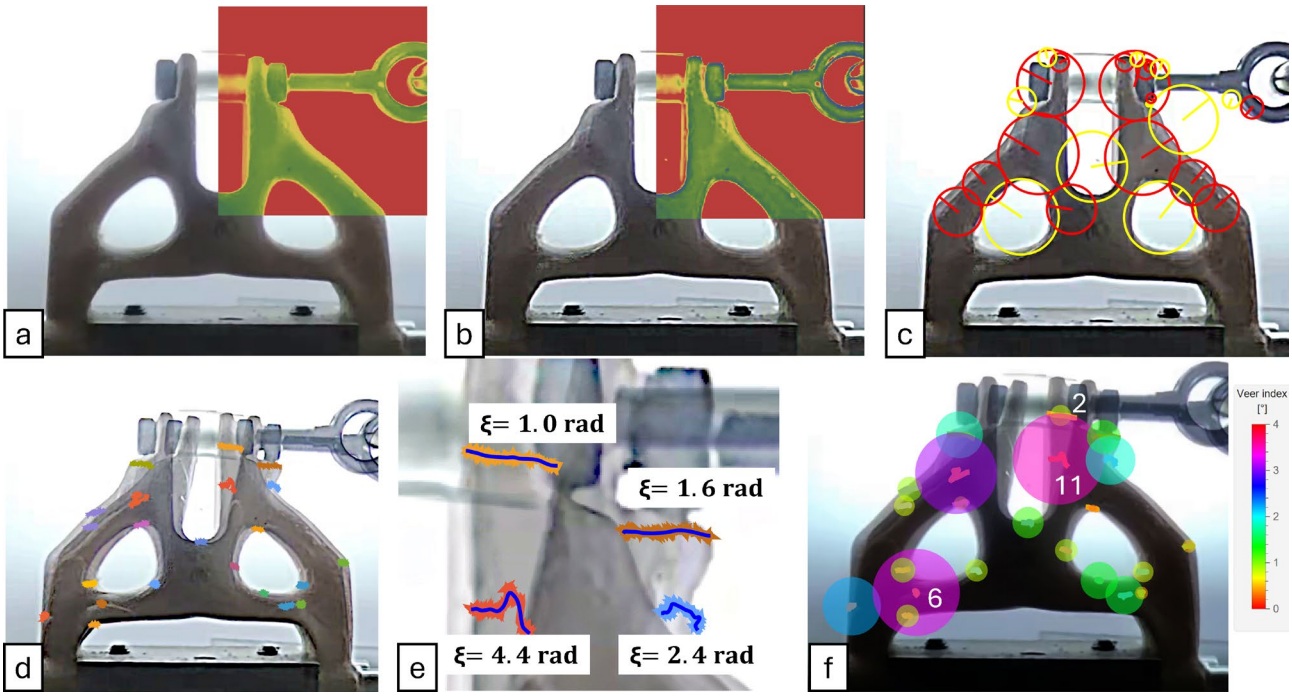

Fig. 7 Digital image analysis of non-standard test: original (a) and enhanced image (b), keypoints (c), feature tracks (d), veer indexes applied to smoothed tracks (e), final graphical representation (f).

The time evolution of the veer index is now analyzed. For the purpose the trajectories 2, 6 and 11 indicated in Fig. 7f are processed. The features 2 and 11 are selected because they both present a long path while the former is smoother than the latter thus leading to lower veer index. The trajectory 6 is shorter because it is close to the constraints and exhibits a final veer index comparable to the trajectory 11 one. In Fig. 8 the veer index as a function of the time for the three trajectories is shown. The evolution of the veer index 2 does not present high slope increment and the correspondent feature is not affected by observable local failures. Conversely, the features 6 and 11 show critical local events as underlined by the before and after images in Fig. 8. The veer index of the trajectory 6 presents a sharp slope increase corresponding to the local failure of the correspondent tracked feature at time 26.2 s, as already reported in Fig. 6. Similarly, trajectory 11 shows two high slope increments related to different observed events at 31 s and 39 s. The local failure events of the tracked features are correctly detected by the veer index slope changes.

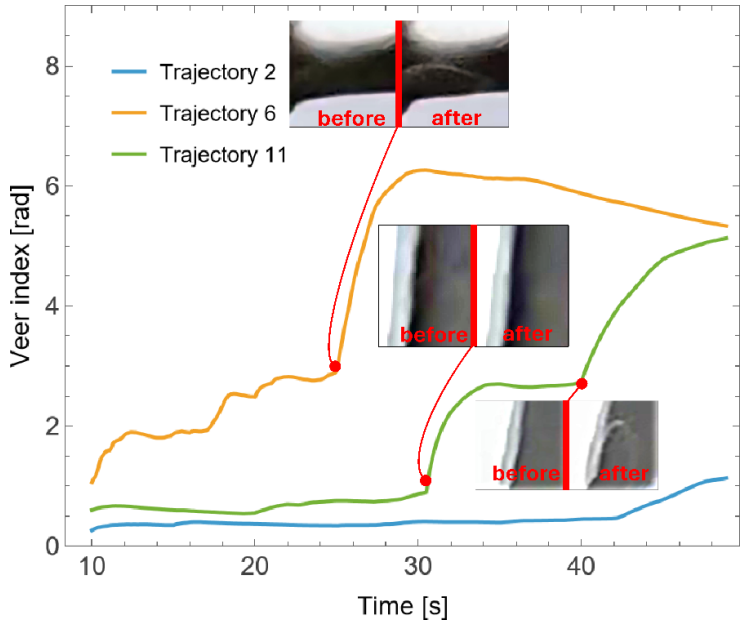

Fig. 8 Veer index time evolutions

In order to mitigate these localized failures, a modification has been provided at manufacturing stage by focusing on a global parameter, namely the rectilinear infill. Fig. 9a shows the results of different infill densities: 5%, 10% and 25%. The 20-PEEK-F10 specimen confirms the general behavior observed for the 22-PEEK-F10 sample, exhibiting a peak load of 820.9 N at a displacement of 4.5 mm, corresponding to an estimated structural stiffness of 182.4 N/mm. The plateau length increases by 167% compared to the previous case. The end of the second region can be placed at the first severe failure occurring at 10.3 mm. After this event, the structure undergoes a reorganization, and the load increases. The 27-PEEK-F05 specimen differs from the other specimens because of its lower infill density (5%). The reduction in infill density leads to a decrease in the maximum load, as well as to a reduction in structural stiffness. The plateau length is comparable to that of the 22-PEEK-F10 specimen. The 25-PEEK-F25 and 26-PEEK-F25 exhibit an expected higher strength than the others. The non-linear quasi-static interval is negligible so the load after this point abruptly plunges showing a brittle behavior. A final observation regarding the 25% infill specimens is the absence of a load plateau region associated with local failures and subsequent structural reorganization. Structures exhibiting this behavior can therefore be classified as brittle. The DIP methodology, which results are reported in Fig. 9b, highlights the critical regions of the specimen: no reasonable criticality is present in the component top and in the right part, whilst the left part is subjected to a sudden failure evidenced by the large red circles proportional to the veer indexes.

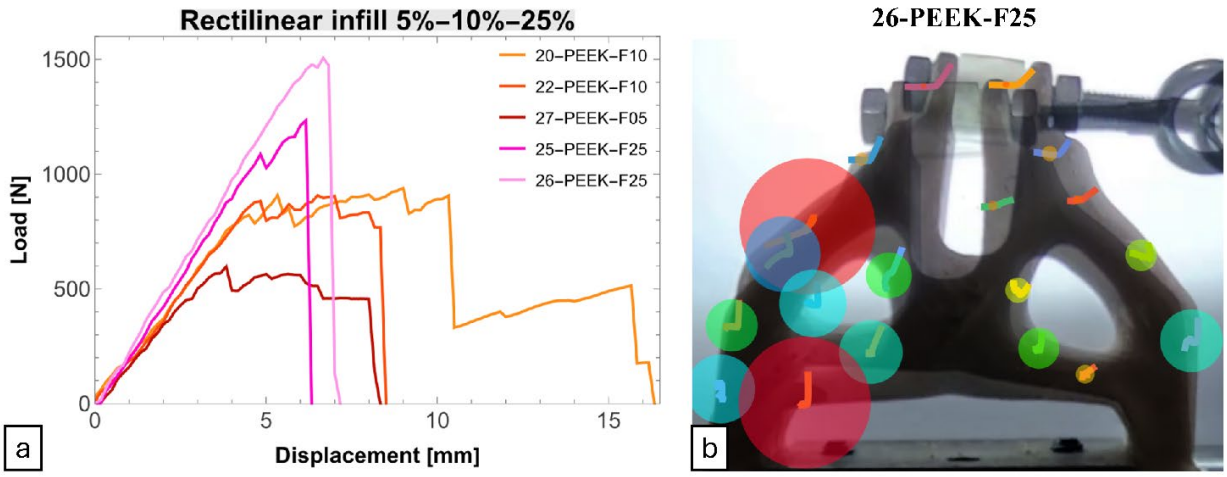

Fig. 9 Load-displacement curves of specimens fabricated with rectilinear infill (a), Graphical representation of the evaluated veer index onto the 26-PEEK-F25 specimen (b)

The SLAM approach adopted in this work allowed to locally redistribute the infill. The methodological steps are reported in Fig. 10. The generation of the points and the related flow lines (Fig. 10a) are tridimensionally thickened in pipes (Fig. 10b); the external skin, created with a desired thickness (Fig. 10c), is assembled together with the solid pipes in the final geometry of Fig. 10d.

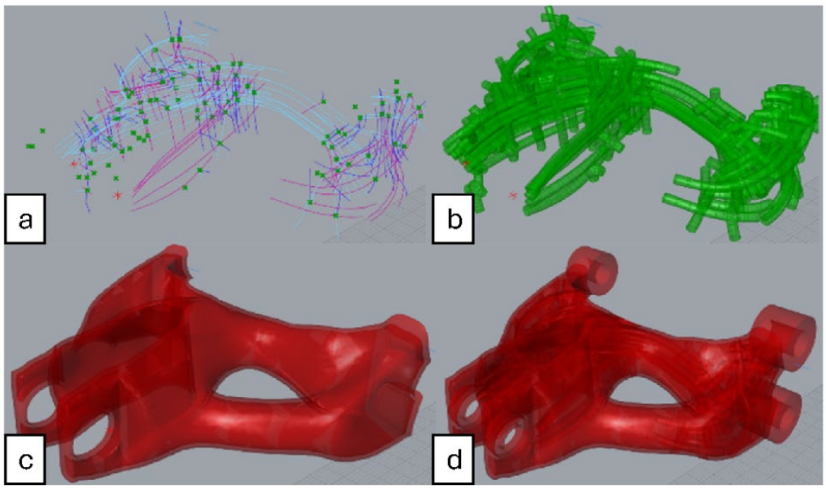

Fig. 10 SLAM geometry generation: points and flow lines (a); solid pipes (b); outer skin (c); final assembly (d)

The curves of specimens 23-PEEK-ASY and 28-PEEK-ASY are shown in Fig. 11a. Both linear and non-linear quasi-elastic regions can be observed; the 23-PEEK-ASY has a load plateau larger than the 28-PEEK-ASY specimen. SLAM specimens and the 25% infilled ones have similar mass. The 25-PEEK-F25 and the 26-PEEK-F25 show higher peak load and slightly higher structural stiffness than the SLAM specimens. The DIP analysis on the 23-PEEK-ASY indicates a critical zone on the left foot of the specimen (Fig. 11b): one big circle surrounded by two smaller ones. The rest of the structure is characterized by negligible variation of the track vector phase. Hence, a modification of the SLAM design has been investigated. The 24-PEEK-SYM and 29-PEEK-SYM specimens have been designed by adding a dense distribution of structures in the evidenced critical zone leading to a symmetric counterpart. The force displacement curves are shown in Fig. 11a: the specimens exhibited a more brittle behavior with respect to the previous ones. From the DIP results a more homogeneous distribution of vector phase variation can be observed with respect to the symmetric SLAM (Fig. 10c). This result points out that this solution allows for better stress distribution and consequently the critical states are reduced. In fact, from the curves it is well evident that many initial damages occur in the asymmetric specimens before the load leak is reached whilst in the symmetric ones the quasi-elastic behavior is shown till the break.

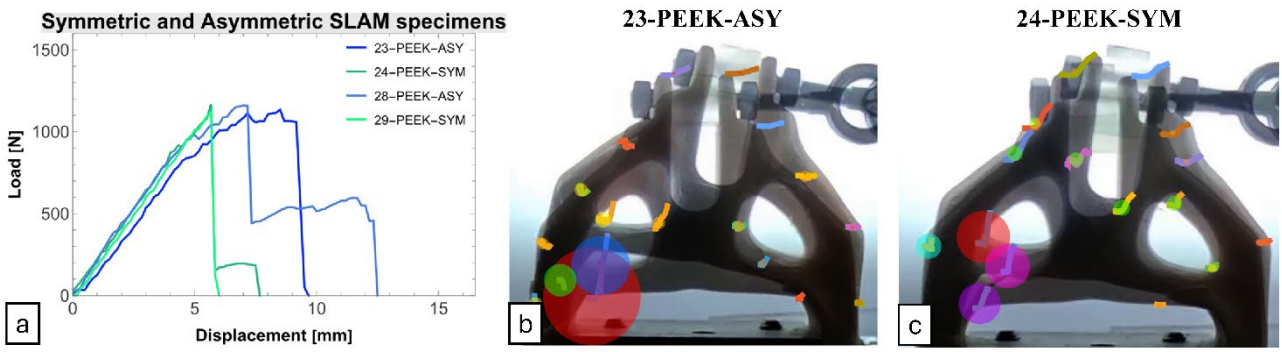

Fig. 11 Load-displacement curves of specimens designed through SLAM (a), graphical representation of the evaluated veer index onto the 23-PEEK-ASY specimen (b), graphical representation of the evaluated veer index onto the 24-PEEK-SYM specimen (c)

It can be concluded that this methodology provides a better understanding of the design effect on component performance. It indicates where the criticalities take place and allows for addressing the design modification. It exhibits limitations such as the quantification is demanded to an index and far from the identification of the local stress; the measure works when the failure affects the component surface. Benefits can be listed as following: the method allows for saving a lot of resources as compared to the efforts and time an industry or AM service must pay for product or prototype development; information on the component geometry local failure; flexible approach for determining the behavior on a specified load range.

Conclusions

This paper investigates a non-standard testing methodology that combines mechanical testing with DIP. Through feature tracking, local mechanical information is extracted from PEEK components fabricated by FFF. The proposed methodology enables the evaluation of local failure mechanisms that cannot be individuated by global load–displacement data alone. Based on the results, the conclusions can be highlighted as in the following:

- As expected, the infill density in components fabricated with rectilinear infill strategy affects mechanical response, including maximum load, structural stiffness, and the final failure behavior. Low infill densities lead to reduced stiffness, and lower peak load, and promote a ductile-like response characterized by load plateaus with multiple localized failures before the structure collapse. Conversely, high infill densities result in brittle behavior, and the absence of a load plateau.
- Without DIP, non-standard mechanical tests provide partial information. Only the structural global response is given, failing on recognizing the onset, location, and evolution of local damage mechanisms. DIP analysis introduces additional information through the proposed phase variation index of the displacement vector field. This indicator allows the identification of regions characterized by nonlinear deformation and failure events. Through this method, the diagnostic capability of the non-standard mechanical test can be enhanced without additional sensors.
- The application of the measurement methodology to SLAM designed components highlights its effectiveness in material distributions. For SLAM specimens, the DIP analysis reveals differences in local failures between asymmetric and symmetric designs, enabling the identification of critical zones. A better understanding on the local failures type and spatial distribution is particularly valuable for complex AM geometries, where standard tests on simple geometry are hardly transferable.

In conclusion, the feedback resulting from the proposed methodology enables specific design interventions. Critical regions, if correlated with specific geometric or filling features, can be redesigned concentrating the design efforts. The results show how the integration of non-standard mechanical testing with DIP can provide a tool to address AM design toward improved and more reliable mechanical performance.

Further developments of the proposed approach will regard the refinement of the descriptor and the extension to more outcome parameters. The goal will be to provide more detailed information about the type of criticality that occurs. Another important intervention will be the deepening of the indexes evolution and their analysis in term of process control. Future research direction will be the application of the method to the monitoring of components during operation. With continuous technological advancements novel monitoring techniques are expected to emerge and imaging shows promising tools for providing richer data to improve the knowledge of AMed components before and after their introduction in the mechanical systems.

Funding

Financed by the European Union—NextGenerationEU (National Sustainable Mobility Center CN00000023, Italian Ministry of University and Research Decree n. 1033–17/06/2022, Spoke 11-Innovative Materials & Lightweighting). The opinions expressed are those of the authors only and should not be considered as representative of the European Union or the European Commis-sion’s

official position. Neither the European Union nor the European Commission can be held responsible for them.

References

[1] A.E. Tetteh, J.A. Smith, H. Spece, D.A. Porter, M.A. Di Prima, S.M. Kurtz, Optimization of fused filament fabrication process parameters to improve the compressive properties of PEEK and PEKK biomaterials, J. Mech. Behav. Biomed. Mater 173 (2026) 107203

[2] G. Sacks, V. Shah, L. Yao, C. Yan, D. Shah, L. Limeta, V. DeStefano, Polyaryletherketones: Properties and applications in modern medicine, Biomedical Technology, Volume 6 (2024) 75-89

[3] E. Altiok, B. Berg-Johansen, S. Lovald, S.M. Kurtz, Applications of Polyetheretherketone in Craniomaxillofacial Surgical Reconstruction, PEEK Biomaterials Handbook (2019) 319-331

[4] J. Day, S.M. Kurtz, K. Ong, Isoelastic PEEK Implants for Total Joint Replacement, PEEK Biomaterials Handbook (2019) 343-366

[5] B. Berg-Johansen, S. Lovald, E. Altiok, S.M. Kurtz, Applications of Polyetheretherketone in Arthroscopy, PEEK Biomaterials Handbook (2019) 291-300

[6] P. Patel, A.A. Stec, T. R. Hull, M. Naffakh, A.M. Diez-Pascual, G. Ellis, N. Safronava, R.E. Lyon, Flammability properties of PEEK and carbon nanotube composites, Polymer Degradation and Stability, Volume 97, Issue 12, 2012, 2492-2502

[7] C. Shen, Y. Guo, Z. Shen, F. Yan, N. Zhong, Additive Manufacturing of Aerospace Composites: A Critical Review of the Material–Process–Design Interplay and Prospects for Application, *Materials* (2025), *18*, 4280

[8] A.H. Alami, A.G. Olabi, A. Alashkar, S. Alasad, H. Aljaghoub, H. Rezk, M.A. Abdelkareem, Additive manufacturing in the aerospace and automotive industries: Recent trends and role in achieving sustainable development goals, Ain Shams Engineering Journal, Volume 14, Issue 11, (2023)

[9] M.R. Adibeig, M.A. Saeimi-Sadigh, F. Vakili-Tahami, M.R. Karimani, G. Marami, Quasi-static simulation and fatigue life estimation of fused filament fabrication of polylactic acid specimens using finite element method, Journal of Manufacturing Processes, Volume 106 (2023) 202-213

[10] R.H. Hambali, Kursat Celik, P. Smith, A. Rennie, M. Ucar (2010). Effect of Build Orientation on FDM Parts A Case Study for Validation of Deformation Behaviour by FEA, International Conference on Design and Concurrent Engineering (2010) 224-228

[11] M. Domingo-Espin, J.M. Puigoriol-Forcada, A.A. Garcia-Granada, J. Llumà, S. Borrós Gómez, G. Reyes Pozo, Mechanical property characterization and simulation of fused deposition modeling Polycarbonate parts, Materials & Design, Volume 83 (2015) 670-677

[12] M. Bugatti, Q. Semeraro, Limitations of the inherent strain method in simulating powder bed fusion processes, Additive Manufacturing, Volume 23 (2018) 329-346

[13] J.C. Russ, The Image Processing Handbook, sixth ed. CRC Press, 2011

[14] K.S. Vivek, K. Jitendra, S. Deepika, V. Abhishek, T. Akilan, K.S. Ashutosh, Machine Vision Analysis in Industry 5.0: Fundamentals, Applications, and Challenges, Chapman & Hall, (2026)

[15] A.H. Alavi; M. Feng; P. Jiao; Z. Sharif-Khodaei, The Rise of Smart Cities: Advanced Structural Sensing and Monitoring Systems, Elsevier Science & Technology, Elsevier Ltd., Kidlington (2022)

[16] C. Liu, J. Xu, F. Wang, A review of keypoints' detection and feature description in image registration, Scientific Programming, Volume 2021 (2021)

[17] N. Xu, W. Lin, X. Lu, Y. Wei, Video Object Tracking: Tasks, Datasets, and Methods, Springer International Publishing, Synthesis Lectures on Computer Vision (2024)

[18] L. Meng, W. Zhang, Q. Dongliang, H.S. Guang, T. Lei, H. Yuliang, B. Piotr, Z. Jihong, G. Tong, From Topology Optimization Design to Additive Manufacturing: Today's Success and Tomorrow's Roadmap, Arch Computat Methods Eng 27 (2020) 805–830

[19] Y. Wang, L. Jin, Y. Zhang, P. Hao, B. Wang CAD-integrated stiffener sizing-topology design via force flow members (FFM), Computer Methods in Applied Mechanics and Engineering (2023)

[20] S. Li, Y. Xin, Y. Yu, Y. Wang, Design for additive manufacturing from a force-flow perspective, Materials & Design, Volume 204 (2021)

[21] G. Xu, N. Dai, Michell truss design for lightweight gear bodies, Mathematical Biosciences and Engineering (2021)

[22] G. Xu, N. Dai, S. Tian Principal stress lines based design method of lightweight and low vibration amplitude gear web. Mathematical biosciences and engineering (2021)

[23] K.M.M. Tam, N. Fine, J. Coleman, C. Mueller, Stress Line Additive Manufacturing (SLAM) for 2.5-D shells, Journal of the International Association for Shell and Spatial Structures

[24] D. Yang, D. Di Stefano, M. Turrin, S. Sariyildiz, Y. Sun, Dynamic and interactive re-formulation of multi-objective optimization problems for conceptual architectural design exploration (2020), Automation in Construction (2020)

[25] T.K. Tan, R. Weerakkody, M. Mrak, Video Quality Evaluation Methodology and Verification Testing of HEVC Compression Performance, IEEE Transactions on Circuits and Systems for Video Technology, vol. 26, n. 1 (2016) 76-90